Granular flows : fluidization and anisotropy

Wortel, G.H.

Chapter 6

Giant Heaping in Sheared Anisotropic Granular Media

6.1 Introduction

Most work on granular media focusses on simplified circular (2D) or spherical (3D) particles. However, the particles in granular media encountered in industry and nature usually have more complex, anisotropic shapes. Gaining insight into the behavior of anisotropic particles is therefore practically relevant, but it also enlarges the theoretical understanding of granular materials in general, and leads to novel questions, for example regarding ordering. In this chapter, we describe experiments where we shear granular rods in the split-bottom geometry.

Recently, the interest in granular rods has increased, with most experiments focusing on the role of *vibrations*. Experiments in 3D on rods in a vibrated tube show that the rods align to the walls and form a high density nematic phase [131–134]. Others performed quasi-2D experiments where similar alignment was found [135]. For low packing fractions, large local density fluctuations are found due to a competition between alignment and void formation [136]. Some studies are performed on the *flow* of rod systems. Here, the emphasis is on the time evolution of the alignment of the particles in the shear band [123, 124, 137–139]. A recent review summarizes the work on granular rod systems [140].

In our flow experiments, we observe strong alignment of the particles in the shear band. In addition, we observe the formation of a heap that arises from the center of the system. In Fig. 6.1 we show two photos of the system – one before, and one after the formation of the heap. The peak of the heap can reach heights of up to 50% of the filling height, which makes these surface undulations a very significant effect. The goal of this

FIGURE 6.1: (top) The initial flat surface. (bottom) A vermicelli heap that has grown while we sheared the system.

chapter is to characterize the heaping process and to unravel the physical mechanism responsible for it.

It is well-known that a densely packed granular material *dilates* under shear [18]. It then reaches the so-called critical state with a steady state void ratio or packing fraction, independent of the initial packing [125]. In geology, it is known from experiments that materials consisting of elongated particles also expand under shear [121]; a result that is confirmed in simulations [141]. In both of these cases it is found that shear creates large voids in the packing, which results in a low packing fraction. A competing mechanism in sheared rod systems is that the shear can cause *alignment* of the particles. This alignment can result in an *increased* packing fraction, as observed in rice avalanches [142] and 2D simulations [143]. In general, both dilation and compaction are present in a sheared granular rod system. It then depends on, *e.g.*, the shape of the particles and the flow geometry which of the two dominates. Recent experiments have shown that in a split-bottom Couette geometry, for shallow filling heights, the dilation dominates, even in the shear band where the particles are strongly aligned [139].

We note that there is a vast literature on sheared thermal rods. Kinetic theory predicts that rods can only align in situations of weak local diffusion [144]. In polymer simulations [145] and attractive colloid exper-

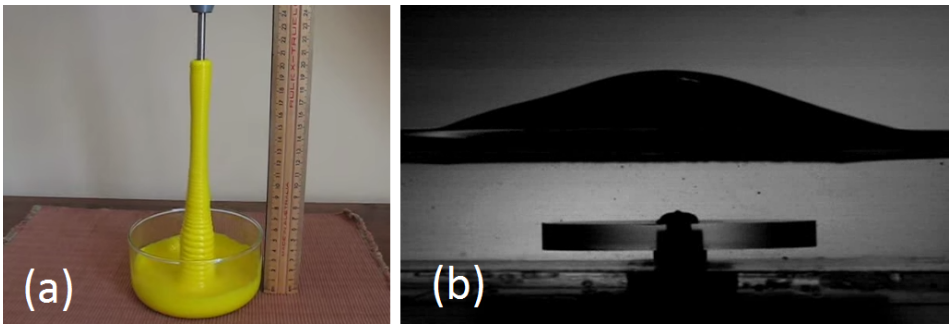

FIGURE 6.2: (a) Traditional rod climbing experiment using a mixture of polyvinyl acetate and sodium tetraborate [147]. (b) Rodless Weissenberg effect using a HASE polymer [148].

iments [146], it is found that the tendency of rods to move out of the shear plane strongly depends on the local $\dot{\gamma}$.

The heaping is reminiscent of the so-called *Weissenberg* effect – see Fig. 6.2. This effect occurs when a spinning rod is inserted into a polymer solution, which as a result will climb up the rod [149]. A similar surface deformation has also been observed with a viscoelastic fluid in the split-bottom geometry [148]. In both cases, the surface deformation is driven by a net centripetal force, which originates from normal force differences in the system. As a consequence, the height of the fluid bump depends on the rotation rate of the rod and goes to zero for slow flows. We note that, whereas similar heaping is found [151–153] for very fast granular flows, our measurements are in the rate-independent regime. We therefore can rule out rate-dependent effects as the cause for heaping.

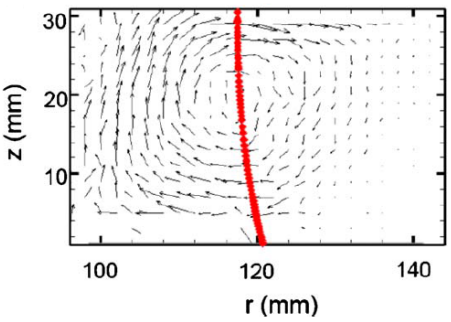

FIGURE 6.3: A vertical slice through the split-bottom cell [150]. The velocity vectors indicate the convection; the red line depicts the shear band.

Experiments on the flow of spherical particles in the split-bottom geometry have shown the presence of *convection rolls* [82, 150, 154, 155] – see Fig 6.3. Similar convection is observed for vibrated sys-

tems [156, 157]. The flow driven convection, which can create either an upwards or a downwards motion in the core, is very slow with respect to the main flow, and much slower compared to our heaping. Nevertheless, as we shall see in this chapter, our heaping process is caused by convection. The essential difference is that the convection is much stronger in a system consisting of elongated particles compared to spherical particles. We believe this to be caused by the misalignment between the particle orientations and streamlines of the flow.

The outline of this chapter is as follows: In Sec. 6.2, we will introduce the setup and explain how the raw data is processed. In Sec. 6.3, we characterize the heaping phenomenon by carefully describing what we observe in the experiments. To unravel how the heaps are formed, we perform experiments with a more complex measuring protocol in Sec. 6.4. To see the motion of the particles below the surface, we performed experiments in an X-ray CT scanner in collaboration with the groups of T. Börzsönyi and R. Stannarius; the results are shown in Sec. 6.5. We end with an outlook where we suggest other interesting experiments concerning anisotropic particles in App. 6.A.1.

6.2 Setup and Methods

6.2.1 Setup

Split-Bottom Cell – The experiments are carried out in a split-bottom cell (see Fig. 6.4(a)) with an outer radius of 110 mm, an inner radius R_s of 85 mm and a height of the container of 120 mm. The inner bottom disk is connect to a SWF 403.559 24 V DC motor, which we use to shear the system. The rate of the motor is controlled by an external duty-cycle controlled, pulsed DC source. The rotating disk is visible from below the system, which enables us to measure its rotation rate, which - for constant settings of the pulse-controlled source - does not significantly depend on the amount of grains in the system. Rice grains are glued to the entire inside of the cell to ensure no-slip boundary conditions.

As we shall see later in this chapter, it was crucial for the discovery of the heaping process that the experiments are performed in the split-bottom geometry. In a Couette geometry, the shear is very localized and

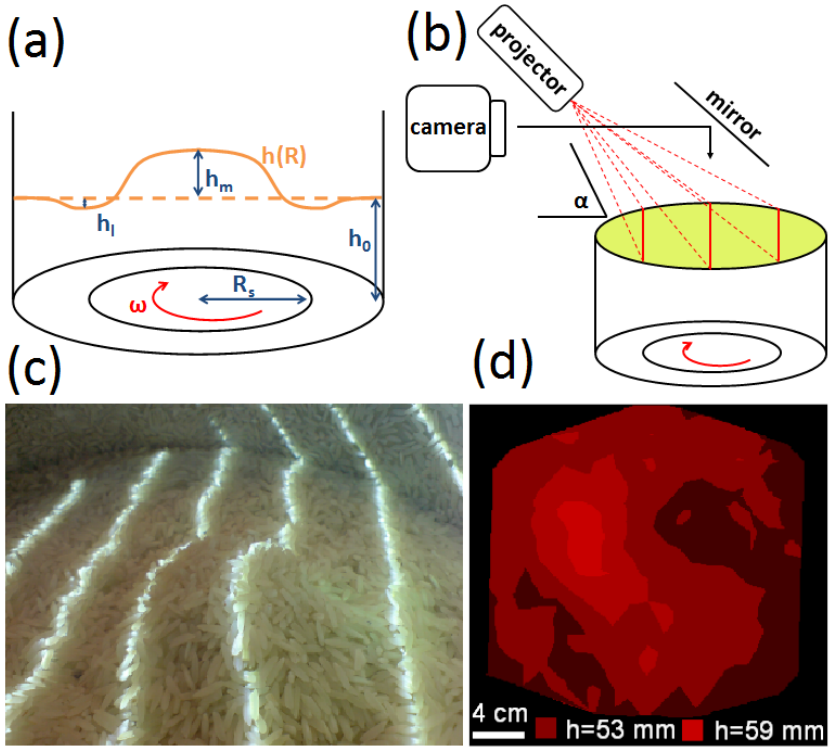

FIGURE 6.4: (a) A schematic of the setup with initial surface (dashed) and steady state heap (solid). The parameters (that are explained in the text) are indicated. (b) A schematic image of the imaging part of the setup. (c) Close up of the heap and the deformed line pattern. (d) The reconstructed surface $\tilde{h}$.

there is no significant heaping. This nicely illustrates, once more, how rich the flow behavior of the split-bottom geometry is.

To image the surface we use a Foculus FO432B camera which is mounted horizontally – see Fig. 6.4(b). We obtain images of the surface of the material right from above using a mirror. To see surface deformations, we project straight lines on the surface using an Epson EB-824 projector. For details, see Sec. 6.2.2.

Particles – Most of the measurements are carried out with long grain "Surinam Rice" particles. The grains have a long axis of approximately

FIGURE 6.5: A picture of the particles that are used for most of the experiment: long grain "Surinam Rice" (left) and vermicelli (right).

7 ± 1 mm and fairly constant short axes of 2.0 and 1.5 mm – resulting in an aspect ratio $Q \approx 4$. Furthermore, measurements are performed using "vermicelli" grains with a very constant diameter of 1 mm and length of 14 ± 3 mm, corresponding to an aspect ratio of about $Q \approx 14$. Most of the vermicelli grains are slightly curved. A sample of these particles is shown in Fig. 6.5.

6.2.2 Methods

In this section we discuss how we measure and reconstruct the particle surface. In addition, we explain how we use the reconstruction to quantify the shape of the heap.

Protocol – Before each run we stir the system by hand to reach a disordered initial state. We proceed by flattening the surface by gently pushing on the system using a circular piece of cardboard. We then start the motor (with a rotation rate of 0.066 rps) and the imaging system, and observe the heap formation.

Surface Reconstruction – To reconstruct the shape of the surface, a series of lines is projected onto the surface using the projector, which is

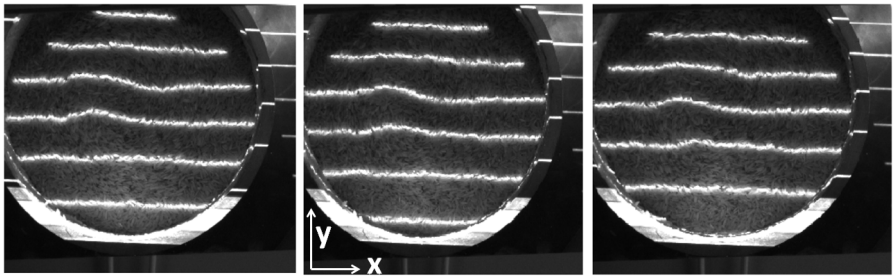

FIGURE 6.6: An example of how we project three series of five or six lines. This method enables us to reach a high spatial resolution without running into tracking limitations.

aimed at the surface under an angle α of 51 ° (for the middle line) – see Fig. 6.4(b-c). The mean distance between the projector and the surface is about 75 cm. The height profile of the surface is recovered from these lines, which, when seen from above, are deformed when the surface shape changes. We take pictures from the top and use these to track the lines using an in-house built IDL-code. To increase the spatial resolution without running into tracking limitations, we project three series of lines (within 0.3 s) consecutively, where the locations of the lines are shifted with respect to each other. The projection of the lines in three series limits our rotation rate to rates below 0.1 Hz; this is not problematic as we have verified to be in a rate-independent regime, so we can perform the experiments at low rotation rate.

An example of three series of lines can be seen in Fig. 6.6. The spacing between the lines in consecutive frames, and thus the horizontal spatial resolution dy, is 10 mm. In the x direction, parallel to the projected lines, for symmetry reasons, we also pick $dx = 10$ mm.

The amount of shear that has been imposed to the system is proportional to the total rotation angle of the bottom disk θ. Because of core precession [77], this can differ from the rotation observed at the free surface. We chose to use the angle of the bottom disk because it is easier to measure than the rotation of the surface (which requires PIV) and because it is kept constant for all the runs. As we shall see in the next section, we have performed experiments where the rotational direction was changed during the run. To plot this without the curve overlapping, we will plot

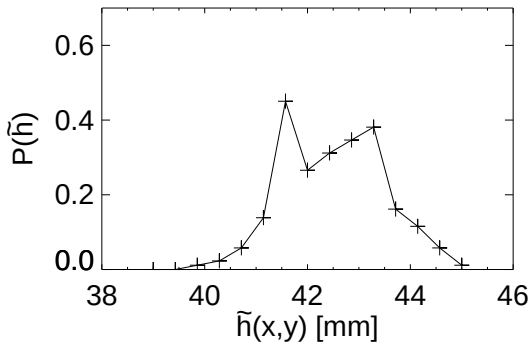

FIGURE 6.7: An example of a pdf of $\tilde{h}(x, y)$ for a flattened surface for $Q = 4$ rice particles.

them as a function of $|\omega|t$, where ω is the rotation rate of the inner bottom disk.

We obtain the local surface height as a function of deflection angle (θ), $\tilde{h}(x, y, \theta)$. For a clear distinction between heaps and depressions we define $h(x, y, \theta) = \tilde{h}(x, y, \theta) - h_0$, where h_0 is the filling height, which is defined as $\langle\tilde{h}(x, y, \theta = 0)\rangle$. In Fig. 6.4(d) we show a color plot that represents the reconstructed surface ($\tilde{h}$).

To investigate the accuracy of surface reconstruction, we prepare the system, as described above, using $Q = 4$ rice particles up to a filling height of 42 mm. We perform the surface reconstruction and plot a pdf of $\tilde{h}(x, y)$ in Fig. 6.7. It can be seen that the spread in h is of the order of 2 mm. We believe that this spread is mostly caused by the rough, grainy surface. From $\tilde{h}(x, y)$, we obtain the actual average filling height $h_0 = 42.7$ mm.

To analyze the orientation of the particles we have an additional fourth stage in our imaging where we just project light on the surface. From these images we can find the local orientation of the grains using PIV analysis.

Interpretation – One key parameter to describe the heaps is their height. Since the maximum value of h is noisy, we define the heap height h_m as the average of the five maximum points of h. Similarly, we define the lowest depression of the surface h_l as the mean over the five lowest points of h. Finally, we look at the average height $\langle h\rangle$. As we shall see in the next

section, the global heap formation process is robust to such an extent that the single parameter h_m is well capable of characterizing the heap.

The parameters that we use to describe the surface undulation are summarized in Fig. 6.4(a).

6.3 Phenomenology

Before studying the heap formation in detail we want to globally characterize the growth process.

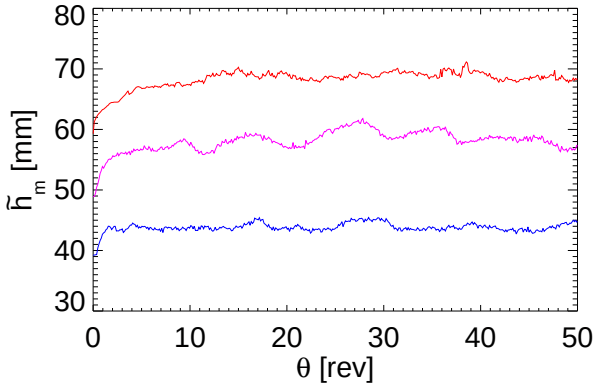

FIGURE 6.8: Evolution of $\tilde{h}_m$ for three different filling heights. It can be seen that for a certain θ, $\tilde{h}_m$ reaches a steady state value $\tilde{h}_M$. The time it takes to reach the steady value decreases with h_0. This data is for $Q = 4$ rice particles.

6.3.1 Growth Evolution

Heap Height $h_m(\theta)$ – In Fig. 6.8 we plot $h_m(\theta)$ for three different filling heights. It can be seen that h_m reaches a maximum value h_M after typically a few rotations. Our data suggests that the process quickly reaches a steady state, in contrast to slow (logarithmic) processes as in the compaction of granular material under vibration [126]. The data also illustrates that the equilibration time increases with h_0/R_s. This can be under-

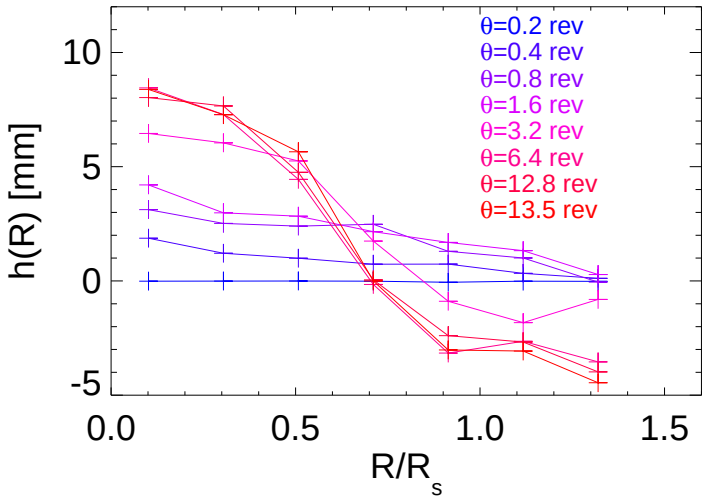

FIGURE 6.9: The surface shape h(R) for $h_0/R_s = 0.46$ and $Q = 14$ vermicelli particles.

stood by realizing that, for large h_0/R_s, the average strain rate and thus the heap formation is slower.

From visual observations of the heap, we see that, even when the steady state height has been reached, particles avalanche down the slopes of the heap. This suggests that the steady state is a dynamical one, where avalanches that decrease h_m and other processes that increase h_m precisely balance.

Heap Profile $h(R, \theta)$ – Because of the cylindrical symmetry of the geometry, we transform $h(x, y, \theta)$ to polar coordinates to get $h(R, \phi, \theta)$. In the case of a rotationally symmetric surface, this can be averaged over ϕ to get $h(R, \theta)$. This provides a simple alternative way to visualize the development of the heaping process.

We show a typical example of its evolution for $Q = 14$ particles in Fig. 6.9. We see that in the center of the system (small R), the heap grows monotonically. In the shear band, at $R/R_s \approx 1$, the height evolution is not monotonic. It seems that the particles first have to align, which requires dilation, but once aligned, the surface drops to a height even below the

original level at $\theta = 0$ [158]. Starting from the curve for $\theta = 6.4$ rev, $h(R)$ maintains it shape, indicating that the system has reached a steady state.

From $h(R)$ we cannot only see whether the system dilates or compacts for certain R, but we can also calculate the total volume of the granular medium by evaluating the integral $2\pi \int \tilde{h}(R) R dR$. As a consistency check, we calculate the volume (for an unsheared packing), and using the total mass of the particles, we find an initial density of approximately 670 g/l. Comparing this to the particle density that we measure to be 1.2×10^3 g/l, we find a packing fraction of 58% – very similar to the ones reported in literature [131, 138].

6.3.2 Aspect Ratio, Shape and Material

We performed exploratory experiments with many different kinds of particles with varying aspect ratio Q and shape. The heaping occurs very robustly for elongated particles with high enough $Q > 3$ – regardless of their exact shape and material. We have done tests and observed heaping for rice grains, slightly bent vermicelli grains (see Fig. 6.5), and perfect PMMA cylinders and metal spherocylinders, both measuring $3 \times 3 \times 12$ mm^3 ($Q = 4$). For short grain rice ($Q = 2$), we did not observe any heaping.

6.3.3 Heap Location

A qualitative difference between the behavior of rice ($Q = 4$) and vermicelli ($Q = 14$) is the precise location of the heap. For $Q = 14$, it is exactly in the center of the system, which results in a symmetric $h(R, \phi)$ that can be averaged over ϕ. For $Q = 4$, the center of the heap is often a few cm off-center (see Fig. 6.4(d)). The heap *does* reach a steady height (Fig. 6.8), but the center of its location corotates with the system. This observation could help in finding the explanation for the heap formation, but it is also a reason, especially when studying $h(R)$, to perform experiments with high aspect ratio particles.

6.3.4 Filling Height Dependence

We study how the heaping effect varies with the filling height h_0/R_s. In the split-bottom geometry, the flow profile changes with h_0/R_s [76]. Therefore, it is interesting to study its influence on the heaping.

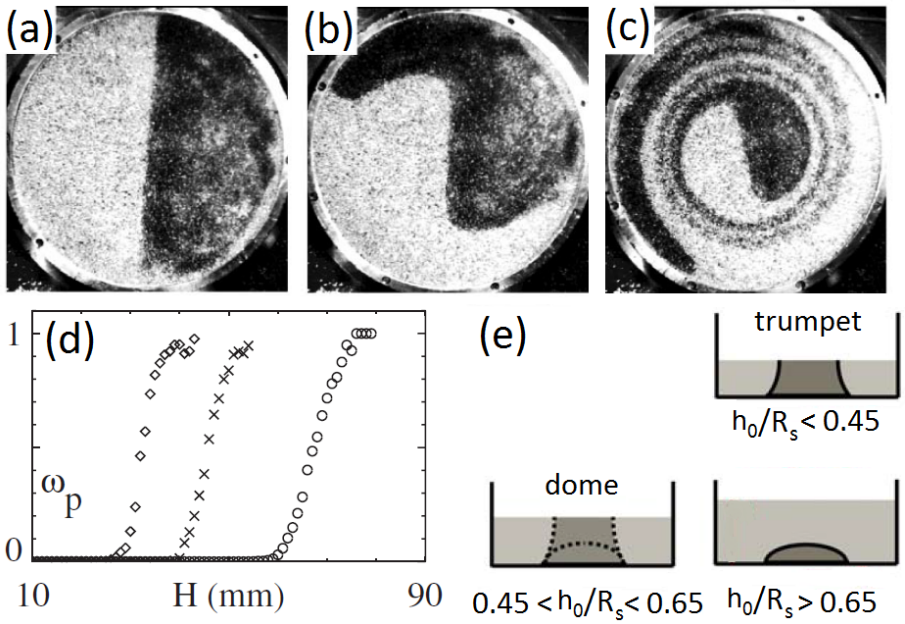

FIGURE 6.10: (a-c) Series of snapshots of top views of the setup, where colored particles sprinkled on the surface illustrate the core precession [77]. (d) Precession rate ω_p as a function of vertical coordinate H for $R_s = 45$ mm ($\diamond$), $R_s = 65$ mm ($\times$) and $R_s = 95$ mm ($\circ$) [77]. (e) The transition in flow structure from shallow to deep flows in the cylindrical split-bottom geometry. In the dark gray region the material comoves with the disk. [76].

Before looking at the heaping data, we summarize the filling height dependence of split-bottom flows in Fig. 6.10. In (e), we show how the flowing region varies with h_0. For shallow filling heights, all the grains in the center of the system comove with the inner bottom disk. For high h_0, there is a velocity gradient in the vertical direction (precession), and particles at the surface have a significantly lower flow rate than the disk. The precession is visualized in (a-c) using colored particles at the surface. Here, the system is driven via the outer wall, and the spiral pattern is a reflection of the angular velocity difference, which increases with R, between bottom disk and surface particles. In (d), we plot the precession rate $\omega_p = 1 - \frac{\omega_s(R\to 0)}{\omega}$, where $\omega_s(R \to 0)$ is the limit of the rotation rate towards center of the top surface [77], as a function of the vertical coor-

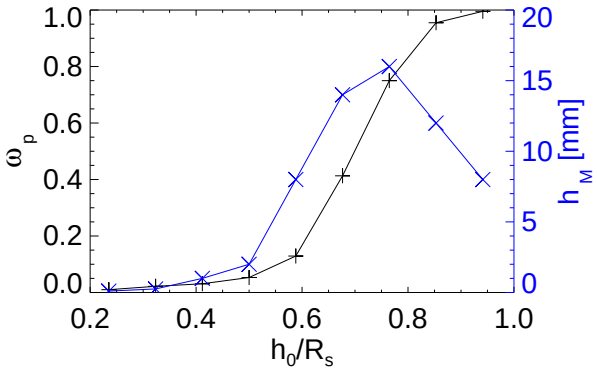

FIGURE 6.11: Filling height dependence of h_M and the core precession ω_p for $Q = 14$ particles.

dinate H. We see that at the bottom, the particles comove with the disk, whereas with increasing H, the precession also increases.

Going back to the heap data, the first question is for which h_0/R_s the effect is the most prominent. In the blue curve in Fig. 6.11, we show the heap height h_M of the heap as a function of h_0/R_s and see that the effect is strongest for $h_0/R_s \approx 0.75$. To compare the heaping with the flow profile, we compare h_M to the precession rate ω_p (plotted in black). We note that we believe the h_0/R_s-dependence to vary with Q.

When we systematically study the filling height, we find the following regimes:

$\boldsymbol{h_0/R_s < 0.5}$ – For low h_0/R_s (trumpet flow), there is no heap formation. The grains on top of the bottom disk just corotate with it ($\omega_p = 0$) and nothing happens in this rigid core. For h_0/R_s close to 0.5, we see a small ridge on the outside of the center, next to the shear band (Fig. 6.12(b)).
$\boldsymbol{0.5 < h_0/R_s < 0.9}$ – For this range in h_0/R_s (dome flow), the shear band starts to close and the grains at the surface rotate slower than the bottom, which results in $\omega_p > 0$. We observe high heaps where the highest point (for $Q = 14$) is at the center of the core (Fig. 6.12(a)).
$\boldsymbol{h_0/R_s > 0.9}$ – For $h_0/R_s > 0.9$, the flow at the surface becomes increasingly smaller, ω_p goes to 1 and h_M decreases. The system does dilate,

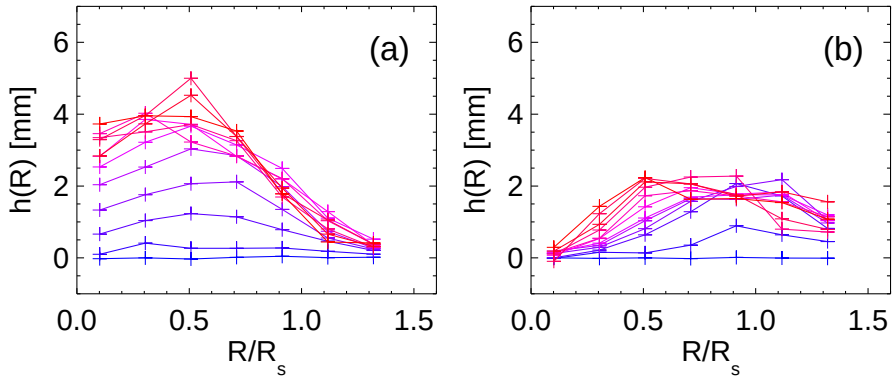

FIGURE 6.12: (a) The surface shape $h(R/R_s)$ for $h_0/R_s = 0.57$ and $Q = 4$ rice particles. The 12 curves from blue to red correspond to θ [rev]=0.2, 0.3, 0.5, 0.8, 1.2, 2, 5, 10, 20, 40, 70, 100. (b) The surface shapes for $h_0/R_s = 0.46$.

which suggests that the dilation in the core also occurs for high filling heights. However, the dilation is averaged out in space so it manifests itself as a homogenous dilation instead of as a heap.

Hence, we find that ω_p and h_M are connected; for filling heights where there hardly is precession, there is also no significant heaping. This suggests that the heaping could be driven by the gradients in angular velocity.

6.4 The Mechanism behind the Heaping

To understand the mechanism behind the heap formation, we perform experiments with a more complex experimental protocol. First, we do experiments where we pause the shear, remove the heap, restart the shear, and see that the heap regrows. Second, we will reverse the direction of the flow, which first, surprisingly, makes the heap disappear and then regrow. Finally, using colored particles, we visualize the secondary convective flow.

6.4.1 Heap Removal

We want to know if the driving mechanism for the heaping occurs continuously, or if it is a transient effect that only works until a steady state

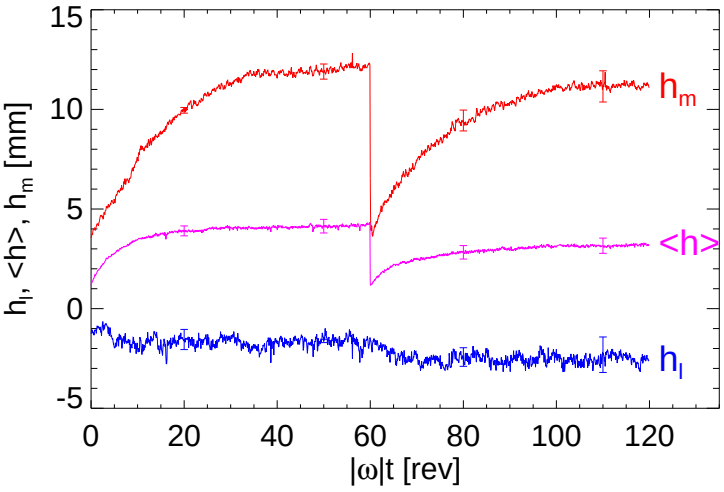

FIGURE 6.13: In this experiment we first grow a steady state heap by shearing the system for 60 rev. The heap height h_m is plotted in red, purple is the average height $\langle h \rangle$ (we see that the system dilates), and blue is the lowest point h_l. After 60 rev we stop the system, remove the heap with a vacuum cleaner, and then restart the flow. We see that the heap grows back. These curves are the average over 10 runs (see error bars) and are for $Q = 4$ particles.

density has been reached in the core. To find out, we perform experiments where we shear the system for 60 rev at 1/15 rps – which is long enough to reach a steady state. We then stop the motor and remove the heap using a vacuum cleaner. After this we restart the motor (in the same direction) and observe what happens. We perform the experiment ten times and average the data for h_m, $\langle h \rangle$ and h_l. The result is shown in Fig. 6.13, with error bars that indicate the standard deviation over the ten runs. It can be seen that a steady heap height is reached well before $\theta = 60$ rev. After we have removed the heap, it grows back at a rate similar to the speed of the first heap formation. The heap reaches a slightly lower height than the first time, which is simply caused by the fact that there are now less particles in the system. From $\langle h \rangle$, we see that the system dilates. This is in accordance with the findings of Wegner *et al.* [139], who reported dilatancy for particles with $2 < Q < 5$ in split-bottom Couette flow.

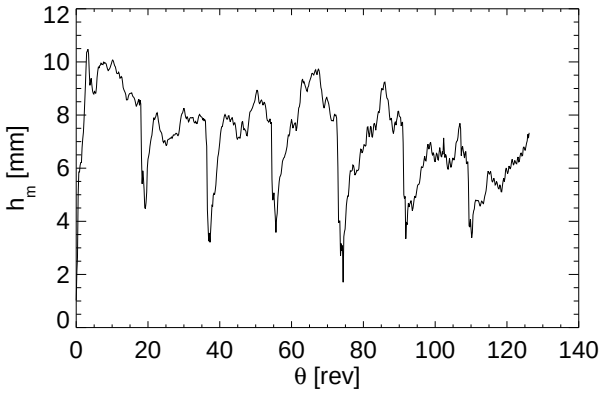

FIGURE 6.14: Evolution of h_m for an experiment where we repeat the heap growth and removal seven times. Every time we remove the heap, it grows back (until a filling height is reached where we never see heap formation). We can therefore conclude that the heap formation process is not a transient effect. This data is for $Q = 14$ particles.

We have performed an exploratory measurement, where we repeat the heap removal multiple times in a single experiment. The evolution of h_m is plotted in Fig. 6.14. After each time we remove the heap, it grows back – until a filling height is reached where no heap formation occurs. Note that the data in Fig. 6.14 is more noisy than the data in Fig. 6.13 because the latter is the average over 10 runs, while the former is only a single run.

The observation that the heap regrows after removal strongly indicates that the heaping process is continuous and not a transient dilation effect.

6.4.2 Reversal

To learn something about the structure of the packing, we perform experiments where we reverse the direction of the flow. We first shear for 53 rev at 1/15 rps to reach a steady state heap, and then reverse flow direction. From the results that are plotted in Fig. 6.15(a) (averaged over ten runs), it can be seen that the heap collapses very fast when the flow is reversed. After the collapse, the heap has completely disappeared and the center of system even shows a small dip compared to the shear band (Fig. 6.15(b)). When we keep shearing after the collapse we see that the heap grows back, at a speed similar to the initial growth rate. After 53 more revolutions, we

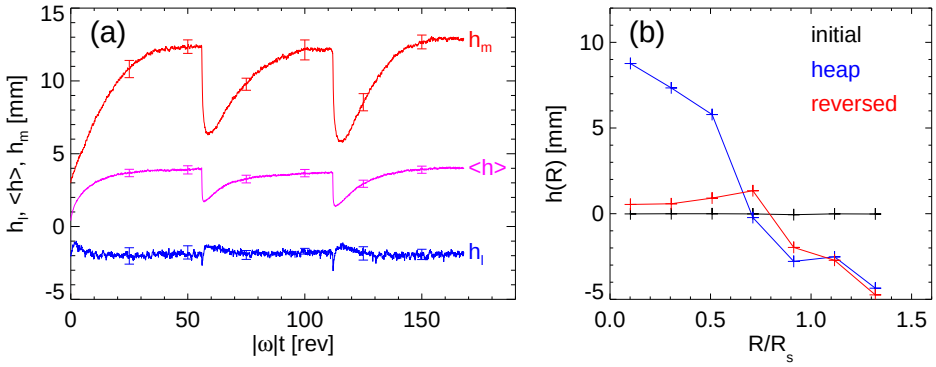

FIGURE 6.15: (a) In this experiment we shear for 53 rev, then shear in the other direction for 53 rev, and then reverse again and shear for 53 rev. Upon reversal, the heap first abruptly disappears and then grows back. This data is for $Q = 4$ and is averaged over ten runs. (b) The surface profiles $h(R)$ for the initial surface (black), the steady state heap (blue) and the collapsed heap after reversal (red). This data is for $Q = 14$.

reverse the flow direction again, and observe the same behavior. From this experiment we can conclude that the packing in the core of the system is anisotropic. In practice, this could mean that the sheared particles leave empty voids behind, which they can easily reoccupy if the direction of shear is reversed.

6.4.3 Convection

The observations that the heap regrows after removal and that particles avalanche down the slopes of the heap, suggest that the heaping is caused by a continuous convective motion that pushes the particles upwards in the center of the system. We test this picture in a simple experiment using colored particles. In this experiment, we prepare the system by putting a layer of colored beads in the core at a certain depth below the surface. When we start shearing the system, we see that after a certain – burying depth-dependent – amount of rotations, the colored particles arise at the surface. When repeating this experiment with spherical particles, we do not observe colored beads at the surface, even after 100 rotations. Using a vacuum cleaner we find that they are still located at their initial position.

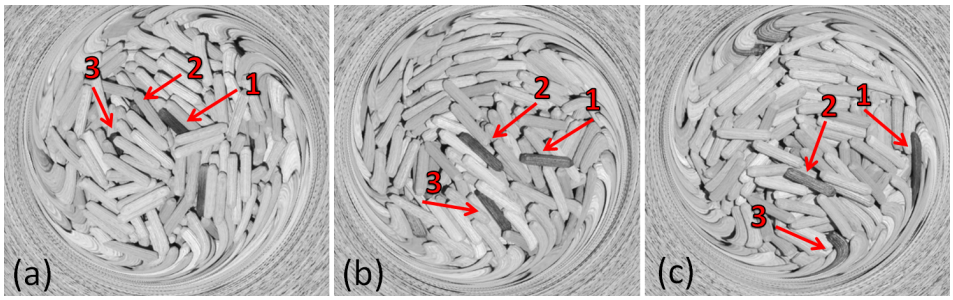

FIGURE 6.16: Three snapshots of continuous heaping. The images are affinely corrected which explains why the sides of the images are blurred. In (a), there are three dark tracer particles rising to the surface, in (b) they are falling down the slope of the hill and in (c) two of the particles disappear in the shear band. This is work in collaboration with T. Börzsönyi.

To visualize the particles that avalanche down the heap, we (in collaboration with T. Börzsönyi – see next section) perform experiments with wooden pegs and make a video of the surface. Using PIV, we correct the frames of this video for the affine motion of the core, so that we can easily see the motion of each individual particle. In Fig. 6.16 we show three snapshots of the video. The blurred outside of the pictures is caused by the affine correction which is only set to correct the motion of the inner part of the system. In (a), there are three dark tracer particles rising to the surface, in (b) they are falling down the slope of the heap and in (c) two of the particles disappear in the shear band. The cyclic raising and disappearing of the tracers particles is a clear visualization of the convection.

6.4.4 Conclusion

From the experiments that are described in Sec. 6.3 and 6.4, we can conclude several things about the heap formation.

From the filling height dependence we learn that heaps only reach a significant height when there is precession. It is easy to imagine that, when there is no precession, the core is not "fluidized" enough to allow heaping. On the other hand, this could also indicate that the gradient in the angular velocity actually drives the heaping. The amount of precession depends on R [79], and there is more shear between horizontal planes

as R increases towards R_s. This could explain why the heap is off-center for $Q = 4$, and why we only see a ridge on the inside of the shear band for low filling heights.

Whereas the heap formation is a robust effect that we find for many different particles with $Q > 3$, it is less clear how the surface profiles $h(R)$ and the local densities of the system vary with particle shape. Fig. 6.12(a) and Fig. 6.13, both for $Q = 4$ particles, suggest that the shear band as well as the core dilate under shear. In contrast, Fig. 6.9 for $Q = 14$, suggests that in the shear band, alignment dominates and the packing compacts, whereas in the core, the dilation wins and the volume expands. We have not studied this systematically and cannot offer precise statements.

The facts that the heap regrows after it has been removed, and that the particles rise to the surface of the heap and then avalanche down its slopes, suggest that the heap formation is caused by convection. In the next section we will study this in more detail using 3D data which is acquired via X-ray tomography.

6.5 3D X-ray CT Tomography

To be able to see the flow and orientation of the particles below the surface, we perform heaping experiments in an X-ray CT scanner in collaboration with the groups of T. Börzsönyi (Budapest) and R. Stannarius (Magdeburg) [123, 124, 137–139].

6.5.1 Setup and Methods

The experiments are performed in a split-bottom cell with an outer radius of 19.5 cm. The inner disk is attached just above the bottom of the container and has a radius of 13 cm and a thickness of 6 mm. In this setup, we shear the particles by rotating the side wall and the outside of the bottom disk. This is in contrast with the setup that was introduced in Sec. 6.2.1, where we drove the system via the inner disk. The reason for this originates from the fact that, because of the CT scanner, the setup cannot contain metal parts and has to be driven by hand. However, there is no difference between rotating the bottom disk or the outer wall in the quasi-static regime in which we measure. The cell is filled to a filling height

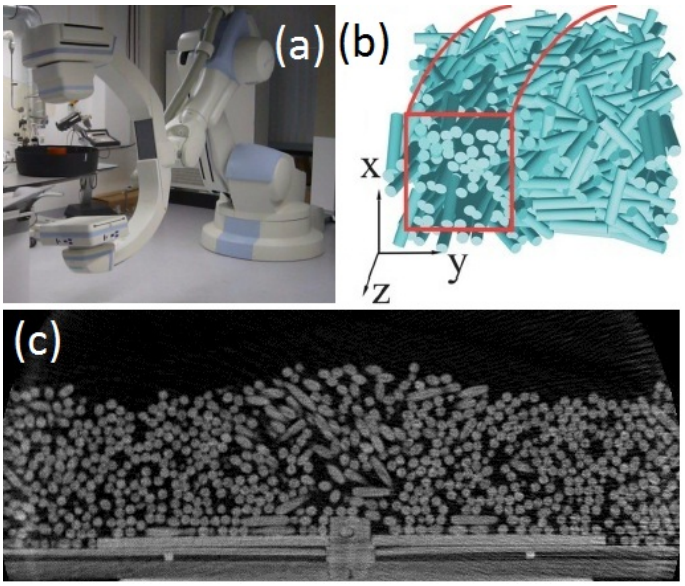

FIGURE 6.17: (a) A picture of the setup placed in the scanner. (b) Visualization of the position and orientation of the particles as reconstructed using a tracing program [138]. (c) An example of a slice through the system made with the X-ray tomograph.

$h_0/R_s = 0.54$ with cylindrical wooden (IKEA ®) pegs with dimensions $2.5\times0.5\times0.5$ mm^3.

The scanner is a medical X-ray angiography machine (Siemens Artis zeego) at the INKA lab, Otto von Guericke University, Magdeburg. It consists of a rotational C-arm based X-ray source mounted on a high-precision robot-arm with a flat-panel detector, featuring high resolution whole volume computer tomography [138]. We make a scan after each 1/16 of a rotation and obtain a spatial resolution of 0.49 mm/voxel – which is significant to identify individual particles. A picture of the scanner and the measuring cell is shown in Fig. 6.17(a).

In Fig. 6.17(c) we show an example of a slice obtained by the X-ray device. From these images we can extract local densities (by simply thresholding the image and counting the light voxels), and particle orientations (via PIV). We can also track each individual particle, and obtain its precisely location and orientation – see Fig. 6.17(b).

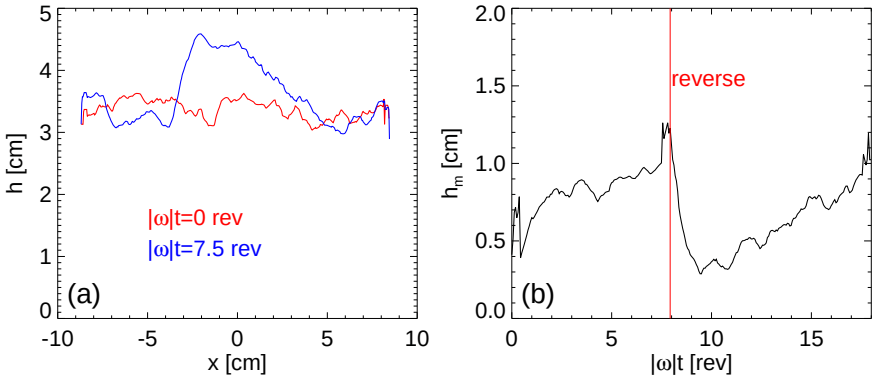

FIGURE 6.18: (a) The shape of the initial surface (red) and after 7.5 rev (blue). (b) h_m for a run where we reverse the direction of the flow.

6.5.2 Results

To get a first impression of the data, we threshold the images that correspond to the slice through the center of the cell (Fig. 6.17(c)), and find the boundary of the packing to recover the shape of the surface (Fig. 6.18(a)) and the heap height (Fig. 6.18(b)). The contrast between the black background and the white particles is large enough so that we can find a threshold value in between the intensity of the particles and the background. This way, we count the percentage of white voxels and obtain a packing fraction of roughly 65%. By finding the height of the packing, h, as a function of the horizontal coordinate x, we recover the surface shape $h(x)$ and heap height h_m. Fig. 6.18 shows that the global heaping behavior is similar to the results reported in Sec. 6.3.

In Fig. 6.19 we show de density Φ (color) and velocity (arrows), obtained by PIV, as a function of R and z. The data is averaged over ϕ and 83 scans of the full system, which corresponds to approximately 5 rotations, all in steady state. In the density field we not only observe the shape of the heap, but also that the density is slightly lower in the shear band than in the core. In the shear band, $\dot{\gamma}$ is higher than in the core, so the data suggests that, for these particles, a higher $\dot{\gamma}$ favors dilation. This is consistent with our results of Fig. 6.9 and Fig. 6.12, which showed that, for $Q = 4$ particles, dilatancy is dominant in the shear band.

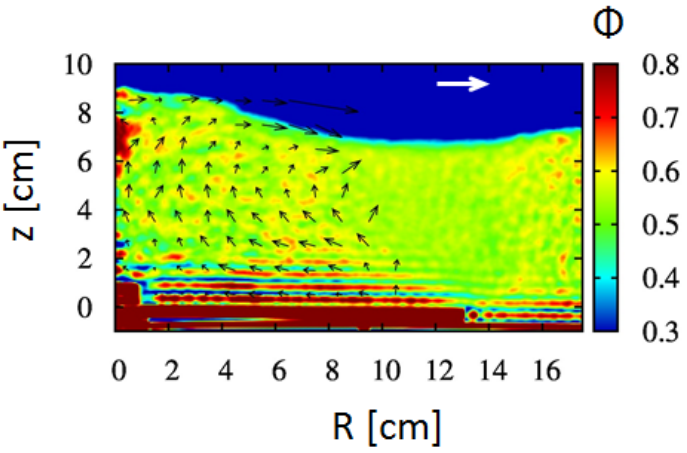

FIGURE 6.19: Density Φ (color) and velocity (arrows) as a function of R and z. The data is averaged over ϕ and 83 scans of the full system, which corresponds to approximately 5 rotations, all in steady state. The density field shows that the density is slightly lower in the shear band than in the core. The velocity field shows a clear convective roll that pushes the particles upwards for small R. For large R, we cannot do PIV because the particle displacements in between two scans are too large to see which particle corresponds to which particle in between two frames. The white scale arrow represents a convection speed of 0.055 cm/rev, which is 1.4×10^{-3} times the main velocity of the grains - in the shear band just outside the inner disk - that corotate with the outer wall.

The velocity field, visualized with the arrows, shows a clear convective roll that pushes the particles upwards at small R. At the top of the heap, the particles avalanche down the heap with relatively high velocity, just as observed in Sec. 6.3.

We continue our analysis by obtaining the orientation tensor T:

$$T_{ij} = \frac{3}{2N} \sum_{n=1}^{N} [l_i^{(n)} l_j^{(n)} - \frac{1}{3}\delta_{ij}] \,, \tag{6.1}$$

where $l^{(n)}$ is a unit vector along the long axis of particle n [123]. The eigenvalues of T; T_{rr}, $T_{\phi\phi}$ and T_{zz} correspond to the amount of alignment in the radial, tangential and vertical direction. A value of 1 corresponds to perfect alignment, a value of -0.5 to an alignment in one of the other two

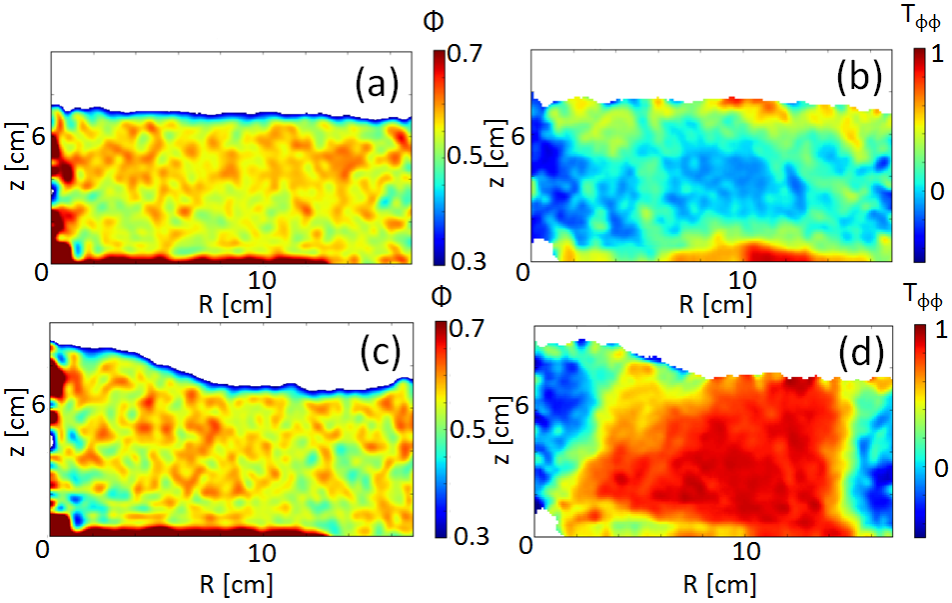

FIGURE 6.20: The density field (a) and eigenvalue $T_{\phi\phi}$ of the orientation tensor (b) for the initial packing and for the packing after 10.5 rev when a heap has formed (c-d). (a) and (c) show that the density has become slightly lower when the heap has formed. (b-d) show that the difference in alignment is enormous.

directions. We find that the alignment in the tangential direction ($T_{\phi\phi}$) is the strongest. In Fig. 6.20 we show the density Φ and $T_{\phi\phi}$ before and after the formation of the heap. It can be seen that the density is slightly lower when the heap has formed, but the difference is small. On the contrary, the difference in alignment before and after the flow is enormous. Initially, the particles are not aligned, but after a shear of 10.5 rev, the particles are aligned in the flow direction in a large part of the system.

6.5.3 Origin of the Convection

Now that we have clearly seen that the heaping is the result of convection, we want to know what drives the convection rolls. There are strong indications that the heaping process is related to the breaking of symmetry in the system. We note that, irrespective of the shear direction, the convec-

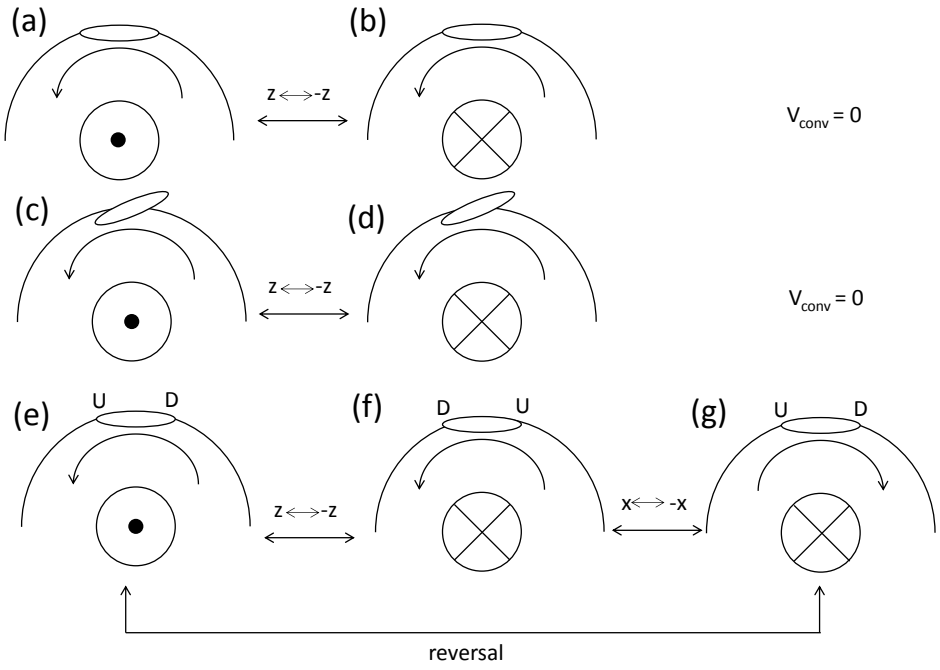

FIGURE 6.21: Using a schematic representation of the particle orientation, shear direction and convection direction, we investigate which particle orientation effect is allowed to cause the heaping by symmetry (see text).

tive flow is always upwards for low R. However, when we reverse the flow direction once a heap has already grown, the convection initially works in the inverse direction (Fig. 6.15). This suggests that the main flow leads to orientation of the grains, which is crucial to drive the secondary flow – something that is absent for spherical grains.

Symmetry – To investigate which particle orientation effect could cause the heaping, we identify which effect is allowed by symmetry. The basic idea is as follows: We take the z-reflection of the experiment, and consider whether this changes the direction of the convection with respect to the other properties of the system. If the z-reflection alters only the direction of the convection, and lets the other properties of the experiment

unaffected, then we know that, by symmetry, the speed of the convection, v_{conv}, has to be zero.

Of course, the z-symmetry of the system is broken by both gravity and the shape of the shear band. However, if we reverse the shear direction, the shear band shape and gravity are unaffected, but, initially, the convection does change direction, leading to the vanishing of the heap. Additionally, if the heaping were caused by the gravity or the flow profile, it is expected to also occur for spherical particles – but it does not. Hence, we rule out gravity and flow structure as candidates to determine the direction of the heaping.

We will now consider the symmetry of the directions of the convection and the main flow, and the precise orientation of the particles, where from now on, gravity is neglected. In Fig. 6.21 we show schematic representations of the experiment. The simplest case, where the particles are aligned exactly with the streamlines of the flow, is shown in (a-b). If the situation is reflected in the z-direction, the particle orientation and flow direction remain the same, but the convection changes sign. This means that in this case, the rate of the convection, v_{conv}, must be zero. In (c-d) we consider the case where the particles are misaligned in the horizontal plane. In (c), the front side of particle points *inwards* with respect to the streamline. If we take the z-reflection of this situation, as in (a-b), the misalignment and flow direction stay the same, while the convection does change sign. Again, this implies $v_{\text{conv}} = 0$. In (e-g) we break the z-symmetry by considering particles of which the front side points *upwards* (U) and the back side point *downwards* (D). If we now take the z-reflection (f), the flow direction is unaltered, but the misalignment of the particles - which is now also in the z-direction -, and the direction of the heaping, *do* change. This means that in this case, v_{conv} does not have to be zero, and convection is allowed by symmetry. In (g), we take the x-reflection of (f). Here, the misalignment and flow direction change with respect to (f), but the convection does not. The resulting configuration is the situation that is reached when the flow direction is reversed starting from (e). The misalignment is the same, the flow is reversed and the convection reverses, which results in the initial disappearance of the heap. Hence, a vertical misalignment of the particles is consistent with both a finite secondary flow, and a transient reversal of the secondary flow upon reversal of the main flow.

Earlier analysis of the orientation of the particles in the shear band has shown that the particles indeed do not exactly align with the streamlines of the flow [137]. Instead, the front sides of the particles point *inwards* and *upwards*, where the *average* angles Θ_a and ϕ_a between the orientation of the particles and the streamline are 10° and 5° respectively. In addition, this orientation state is not stable. The particles continuously tumble with a normalized rotation velocity $\omega = d\Theta/d\theta < 0$ for all Θ [137, 159]. To verify our hypothesis that the convection is caused by the vertical misalignment of the particles, we extract $\Theta_a(|\omega t|)$ and $\phi_a(|\omega t|)$ from the orientation tensor T. Since the behavior of the alignment will most likely be different in different parts of the system, we define four different regions where we will monitor the alignment – see Fig. 6.22. The results are shown in Fig. 6.23. In (a), we show the heap height h_m, where the dashed line indicates the moment when we reverse the shear direction. In (b-c) we plot Θ_a and ϕ_a for the four different regions.

By definition, the angles change sign when the flow direction is reversed. The time it takes to reorient is, as expected, different for the eight curves. For instance Θ_a in region C (shear band) reorients relatively fast. We suggest this is because, in the shear band, the shear rate is relatively high. Other angles, such as Θ_a in region D (high up in the core) and ϕ_a in regions A, B and D (everywhere except the shear band), take much longer to reorient. The number of rotations that this orientational transient persists, in particular for the vertical deviation angle ϕ_a (about 5 rev), corresponds well to the time it takes for the heap to start regrowing. This strongly supports our claim that the convection roll is driven by the vertical deviations between the particle orientations and the streamlines.

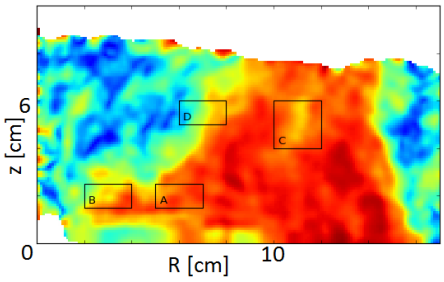

FIGURE 6.22: Indication of the location of regions A, B, C and D where we will monitor the alignment of the particles. The color represents s, which is the largest eigenvector of T.

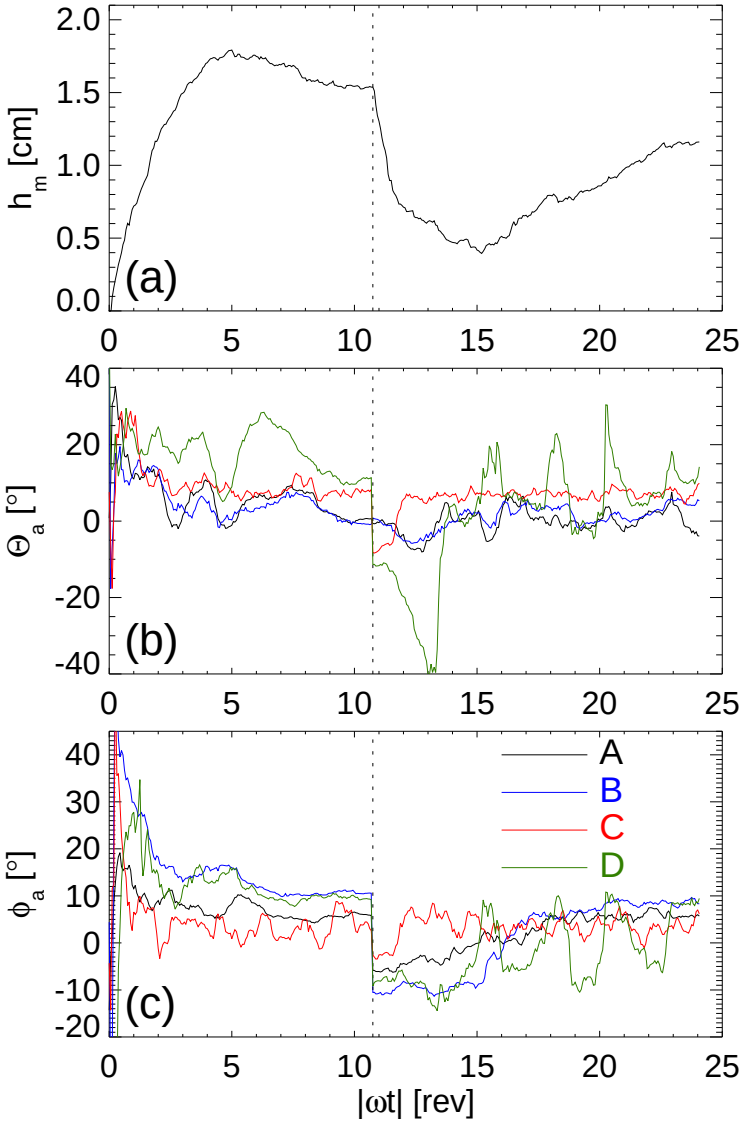

FIGURE 6.23: (a) The heap height h_m as a function of time for a reversal run. (b) The average horizontal deviation angle Θ_a in the four regions as indicated in Fig. 6.22. (c) The average vertical deviation angle ϕ_a. The black dashed line indicates the time when the flow direction is reversed. It can be seen that different parts of the system take a different time to reorient. However, the reorientation times, in particular of ϕ_a, correspond well to the time it takes for the heap to start regrowing.

6.5.4 Conclusion

In this section we have seen that in this alternative setup, that allows for 3D imaging, the heaping phenomenon is the same as in the setup of Sec. 6.3. The PIV analysis of the particles in 3D clearly shows a convection roll that is responsible for the heaping. We have presented a symmetry breaking argument and experimental data that explain how the convection is the result of a vertical deviation between the orientation of the (tumbling) particles and the streamlines of the flow. This argument, in addition, correctly captures the transient disappearance of the heap upon reversal.

6.A Appendix

6.A.1 Outlook

An obvious experiment to do would be to shear oblate (lentils, smarties, coins) particles rather than prolate (rice) ones. We expect these particles to align with the bottom during the filling of the setup, whereas upon shear, the particles in the shear band might orient with the strain rate. Tumbling and heaping could then also occur.

Another experiment would be to shear ratchet-like particles such as wheat grains. A wheat grain is covered with tiny hairs that all point in the same direction. As a result, the grain can easily slide in one direction but not in the other. In a reversal experiment with ratchet particles, we expect a dramatic response after the grains snap from very frustrated positions.

Something that is not yet well understood is how dilatancy and compaction due to alignment compete for different particle shapes and flow geometries. It would be interesting to find an order parameter that indicates how the two effects relate.

More related to the heaping process, it would be interesting to study the details of the convection. In our 3D experiments, we quantified how fast this convection is, but the speed of the convection may vary with the aspect ratio of the particles. Even in experiments without a 3D scanner, this can be measured relatively simply using colored particles. The dependence of the convection speed on particle shape is the subject of current studies in the group of R. Stannarius.